

Explosive Disruption of Polytropes: a One Dimensional Hydrodynamic Calculation

Mark C. Wyman^{1,2*}, David F. Chernoff¹*, and Ira Wasserman^{1,2}*

¹ Center for Radiophysics and Space Research, Cornell University, Ithaca, NY 14853, USA

² Laboratory for Elementary Particle Physics, Cornell University, Ithaca, NY 14853, USA

Submitted 2004 April 23

ABSTRACT

We study explosions of stars using a one-dimensional Lagrangian hydrodynamics code. We calculate how much mass is liberated as a function of the energy of explosion for a variety of pre-explosion stellar structures and for equations of state with a range of radiation-to-gas pressure ratios. The results show that simple assumptions about the amount of mass lost in an explosion can be quite inaccurate, and that even one-dimensional stars exhibit a rich phenomenology. The mass loss fraction rises from about 50 to 100 per cent as a function of the explosion energy in an approximately discontinuous manner. Combining our results with those of other, more realistic models, we suggest that Nova Scorpii (J1655-40) may have experienced significant mass fallback because the explosion energy was less than the critical value. We infer that the original progenitor was less than twice the mass of today's remnant.

Key words: supernovae: general, computational; hydrodynamics

1 INTRODUCTION

A fundamental question in the study of supernovae is the fate of a star subject to an explosion of a given strength: is the star disrupted completely, and, if not, how much of the star is lost and what is the configuration of the matter that remains bound? Many researchers have addressed this question for specific cases of interest using detailed numerical simulation. To our knowledge, a precise quantitative relationship between the strength of the explosion and the fate of the outer layers has not been given before, even for highly idealized stellar models. The potential utility of such a relationship is evident in the analysis of Fryer & Kalogera (2001), where a simple "rule of thumb" is employed to estimate the amount of mass left bound in a supernova, which in turn allows a determination of which high mass stars leave behind neutron stars and which ones yield black holes. The "rule of thumb" used in Fryer & Kalogera (2001) is that a portion (between 30 and 50 per cent) of the explosion energy is effective in directly unbinding the outermost layers of a star; this estimate is based on detailed simulations by MacFadyen et al. (1999) for a set of specific models for the stellar progenitor.

Our goal is to improve the understanding of the disruption process by carrying out hydrodynamical calculations of simple stellar models with a range of explosion strengths,

a range of stellar structures and a range of equations of state. We intend this sort of calculation to complement, not replace, the realistic, detailed simulations that are the current state-of-the-art in this field. Our models do not include the physical complications – density jumps, neutrino transport, and so on – that are important ingredients of realistic collapse and concomitant stellar explosion. Our goal is to incorporate the essential physics – hydrodynamics and gravity – in models that are easy to compute and are useful in the study of supernovae in the same way that the polytrope itself is useful to stellar modeling. Already, our results yield improved versions of the "rule of thumb" which we provide in simple, easily applied, empirical form. Although a host of significant modeling uncertainties of core collapse (hydrodynamic motions in the core, distribution of angular momentum within the collapsing object, neutrino-matter coupling, etc.) remain, our simplified treatment represents an improvement in the determination of the fate of central remnants – providing a convenient bridge between simple assumptions about mass loss and more sophisticated simulations that attempt to model real stars.

Because the principal focus of this work is explosions that do not completely destroy the star, our simulations involve material that falls back onto the remnant. Our results may also be used to determine the accretion rate of the fallback for the case of simple, idealized stellar structures.

There is considerable evidence that a supernova explosion occurred in J1655-40: the atmosphere of its companion is contaminated with elements thought to be formed

* E-mail: wyman@astro.cornell.edu; chernoff@astro.cornell.edu; ira@astro.cornell.edu

only in supernovae (Israelian et al. 1999), and it is likely that the black hole progenitor was considerably more massive than the remnant we see today (Orosz & Bailyn 1997; Shahbaz et al. 1999). There is also some evidence that the J1655-40 system could have remained bound only if it received a substantial kick during or shortly after the formation of its black hole (Mirabel et al. 2002). While our current models are too simple to say anything definitive about any particular system, we believe that the methods employed here could be extended to treat such problems as the initial collapse of the core to a neutron star, the impulse the core received (kicked by one of several physical mechanisms thought to be responsible for high pulsar velocities), and the accretion driving the black hole formation. The mass fallback may trigger the collapse to a black hole as well as pollute the companion's atmosphere. Finally, we note that this subject has been treated before, in a very different perturbative calculation (Nadezhin & Frank-Kamenetskii 1963).

In section 2, we describe the physical set up, while section 3 describes the numerical code. In section 4, we give more detailed results and discuss how the numerical data were analyzed.

2 PROBLEM AND PARAMETER RANGES

We model the supernova as a spherically symmetric explosion in a star that is initially in hydrostatic equilibrium. The pre-explosion stellar structure is a polytrope. We deposit the full energy of the explosion in a small region near the centre of star. Using a finite-difference code we calculate the hydrodynamical evolution. A shock propagates towards the surface and the outer layers of the star may be ejected. If the star is not completely destroyed, some of the matter remains gravitationally bound and we follow the evolution long enough to make an accurate estimate of the mass of the bound object.

We considered a range of initial stellar structures. We varied the polytropic index Γ where $P \propto \rho^\Gamma$. The Lane-Emden equation prescribes the run of density and pressure of the initial model; our choices for $n = 1/(\Gamma - 1)$ span $3/2 \leq n \leq 4$. As is well-known, the polytrope's ratio of central to mean density increases as n varies from 0 to 5. The range subsumes typical main-sequence profiles and extended red-giant structures.

We have considered two equation of state treatments: ideal gas pressure ("EOS M": $P = P_{\text{matter}}$ with a fixed ratio of specific heats γ) and a mixture of gas plus radiation in thermal equilibrium ("EOS MR": $P = P_{\text{rad}} + P_{\text{matter}}$). EOS M is suitable for stars of low mass (dominated by particle pressure at their centres) and weak explosions (such that the post-shock gas is not radiation dominated); EOS MR is needed if there is significant radiation pressure. We infer the temperature profile from the appropriate EOS and the Lane-Emden pressure-density profile. For EOS MR, the chose to limit ourselves to convectively stable, polytropic models. We will discuss the condition for stability in §4.2. To further describe our problem's parameter space, we introduced a new parameter, $s_c = P_{\text{rad}}(r = 0)/P_{\text{matter}}(r = 0)$. As we will show in §4.1, for a given polytropic index n , choosing s_c uniquely fixes the mass of the resulting stellar model. Utilizing this relationship, we can define a stellar

mass scale that scales with the choice of μ for the stellar gas: $M_{\text{scale}} = M_\odot(m_p/2\mu)^2$. We then chose the dimensionless masses of the stars we explode to be $\tilde{m} = M_{\text{star}}/M_{\text{scale}} = 10, 100, 1000$ for a variety of values of n , taking care to remain in the convectively stable range of parameter space. See 1 for details.

We considered a range of explosion energies. Given that we are concerned with analyzing under what circumstances the star is disrupted, we typically considered blasts with $0.1 \leq E_{\text{blast}}/E_{\text{bind}} \leq 1.5$, i.e. energies of the same order of magnitude as a simple dimensional estimate for unbinding. In brief, the results we obtained were as follows.

- The amount of mass lost as a function of explosion energy makes a discrete jump from approximately 50 to 100 per cent in all models, suggesting a point of instability.
- Explosions that do not totally disrupt a star give rise to mass loss curves that, in most cases, scale quadratically with explosion energy

In most of our simulation survey, we did not include any sort of compact object at the core of our explosions. We explored the sensitivity of the mass loss to two unsatisfactory aspects of the idealized polytropic star: our treatment of the inner boundary condition, and the lack of a central compact object. We found that to a large extent the results are unchanged:

- When two extreme inner boundary conditions – a 'vacuum cleaner' core that sucks up any incident material, and its opposite, a hard, reflecting shell – were compared, the mass loss results were virtually identical.
- Adding an appropriately massive central compact object to one particular model resulted in mass loss that had a functional dependence on explosion energy very similar in form to what we found with no central compact star.

Readers primarily interested in further details regarding these results are encouraged to skip to §4.

3 THE CODE AND NUMERICAL TESTS

3.1 Equations

We use the inviscid fluid equations which describe mass, momentum and energy conservation. All calculations are one-dimensional with either a plane-parallel (for testing) or spherical (for testing and simulations) geometry. We advance the fluid state using a finite difference approximation to the fluid equations (Lax-Wendroff, explicitly differenced, 1-D Lagrangian code (Richtmyer & Morten 1967). Shocks are handled with the addition of artificial viscosity. We solve Poisson's equation to determine the gravitational forces on each time step. Details are provided in Appendix 1.

3.2 Tests of hydrodynamics

We tested the purely hydrodynamic capabilities of the code (no gravity) on the Sod shock tube problem (plane-parallel geometry) and on the Sedov blast (spherical geometry). For the Sod test with $\gamma = 7/5$ (as well as for a range of other γ 's), EOS M, and various overpressures ($p_2/p_1 = 10, 100, 1000$) and 1200 zones, we found essentially perfect agreement of

the numerical and analytic solutions except for the shock smearing over $\sim 5 - 8$ zones.

For the Sedov problem, we re-derived the solution given in *Fluid Mechanics* by Landau & Lifshitz (1987), thereby finding the correction to the often remarked upon error (in an exponent) in that book's solution. Appendix 2 gives the full solution. We carried out a number of variants of the basic blast wave simulation in terms of EOS and γ . For flows dominated by particle pressure we compared numerical solutions ($\gamma = 5/3$ and $7/5$ for EOS M) with the analytic similarity solution (with γ matched; see Appendix 2). For flows dominated by radiation pressure we compared several different radiation-dominated numerical solutions ($\gamma = 5/3$, EOS MR) to the $\gamma = 4/3$ similarity solution. The radiation-dominated numerical solutions were generated using cold preshock gas so that the explosions yielded a high Mach number flow and $P_{\text{rad}}/P_{\text{matter}} \gg 1$ in the postshock region. A range of initial radiation-to-matter pressure ratio s and shock energies was considered. A simulation with large constant $s \sim 1000$ and relatively small explosion and a simulation with small constant $s \sim 0.1$ and large explosion both yield a radiation-dominated numerical solution.

The explosion was allowed to expand to well over 100 times the size of the initial “bomb zone” in all cases. Comparisons of EOS M runs with analytic solutions were possible throughout the simulation; comparisons of EOS MR runs with the analytic radiation-dominated similarity $\gamma = 4/3$ solution was meaningful only for the part of the simulation in which radiation pressure dominated matter pressure, approximately 4-5 expansion times. With 800 zones, the Sedov test gave close (2–3 per cent) agreement in the relative density, velocity and pressure of the numerical solution and the analytic similarity solution for both particle pressure dominated and radiation pressure dominated flows except in the central-most region.

Two factors contribute to the discrepancies at the centre. First, the innermost zone was treated as an adiabatic expanding/contracting bubble. The entropy of this zone was incorrect but its mass was so small that its impact on the rest of the solution was inconsequential. The explosion results were found to be almost entirely insensitive to alternative methods of treating this inner zone, provided the treatments were energy conserving. Second, explosive energy was injected in a small, but non-negligible central region (typically the inner 5 per cent of the mass). Departures between the analytic solution and the part of the grid used as the “bomb zone” persisted through the simulation. We also compared two models for the energy injection at the centre. In one, the “thermal bomb,” an excess of thermal energy equal to the desired explosion energy was added by hand to the core (inner 5 per cent of the mass) of the star, essentially creating an out-of-equilibrium hot core that then expanded rapidly out into the stellar envelope. In the other, the “kinetic bomb,” a linear velocity profile carrying the same amount of energy was added to the inner 5 per cent of the mass. Both methods produced identical results outside the “bomb zone.”

3.3 Tests of hydrostatics

With the inclusion of self-gravity forces, we verified that Runge-Kutta integration of the Lane-Emden equations yielded stationary, stable configurations for our time-

dependent hydrodynamic evolution equations (finite difference scheme). We verified the long-lived stability for all polytropic indices and radiation-to-gas pressure ratios adopted in this study. Likewise, we verified that the virial theorem was satisfied by the initial configurations.

3.4 Tests of self-gravitating explosions

In the actual runs of the problem of interest, we further verified that the treatment of the central zone made no discernible difference, that variations in the size of the “bomb zone” (3-10 per cent, for instance), caused only very slight (< 5 per cent) changes to the amount of mass lost in the explosions. We also verified that energy conservation was satisfied (to < 5 per cent).

4 RESULTS

We adopted polytropes for the initial stellar structure with $P = k\rho^\Gamma$. The density and pressure profile is determined by solution of the Lane-Emden equation with the total mass and radius scaled to unity. We refer to this as the dimensionless solution; it depends only upon Γ . The dimensionless density-pressure distributions are the forms used in our computations. In the results, we discuss dimensionless quantities (explosion energy in terms of binding energy, mass loss in terms of the total mass, etc.) so that our results can be scaled to physical situations as needed.

4.1 Scaling of polytropes

Let us first review the scaling of the initial polytropic solution. For given k and $\Gamma \equiv 1 + 1/n$ in the pressure-density relation, it is possible to generate a one-parameter family of scaled solutions with

$$M^{2-\Gamma} R^{3\Gamma-4} = (k/G) f(\Gamma), \quad (1)$$

with $f(\Gamma)$ a dimensionless number depending on polytropic index. We can pretend to construct a polytropic progenitor without radiation pressure, but that is only an idealization that is approximately correct in the limit of a low ratio of radiation to gas pressure. If the gas has an ideal gas equation of state, $P = \rho kT/\mu$, there must be nonzero temperature inside the star, and hence nonzero radiation pressure $P_{\text{rad}} = aT^4$. Under some circumstances, P_{rad} will be low in the progenitor, and even in the ejecta after the star explodes. The explosion of such models with given Γ has a universal mass loss fraction as a function of explosion energy in units of the stellar binding energy.

Imposing a fixed value of the radiation-to-gas pressure $s(r=0) = s_c$ at the centre of the star before the explosion reduces the scaling of the dimensionless solution. Models with a given Γ and s_c still have a universal mass loss fraction as a function of explosion energy. The reason the scaling is reduced is because specifying s_c determines the stellar mass for a given value of Γ independent of k :

$$M = m(\Gamma) M_{\text{Ch}} s_c^{1/2} (1 + s_c)^{3/2}, \quad (2)$$

where $M_{\text{Ch}} = (\hbar c/G)^{3/2} \mu^{-2} = 1.86(m_p/\mu)^2 M_\odot$, and $m(\Gamma) = (45/\pi^2)^{1/2} [f_\rho(\Gamma)]^2 [f_p(\Gamma)]^{-3/2}$, with $f_p(\Gamma) =$

$P_c R^4/GM^2$ and $f_p(\Gamma) = \rho_c R^3/M$, which are both dimensionless functions of polytropic index only. For $n = 3/2$, $f_p = 1.430$ and $f_p = 0.7702$, so $m(5/3) = 6.460$; for $n = 3$, $f_p = 12.94$, $f_p = 11.05$, so $m(4/3) = 9.734$. Thus, from Eq. (1), the combination $kR^{4-3\Gamma}$ is determined given Γ and s_c . Recovering the $s_c \rightarrow 0$ limit is subtle, since it also implies low mass M . Note that we use Eq. (2) to solve for s_c given M , taking $\mu = \frac{1}{2}m_p$. In the low mass limit, this implies $s_c \propto M^2$.

In this paper we will adopt the point of view that k is not known *a priori* and we will allow scaling of the polytropic solution to arbitrary M and R in cases with no radiation pressure. In cases with radiation pressure, although M is determined from Eq. (2), some scaling remains since Eq. (1) relates R and k , given M and Γ , but does not determine either one separately.

4.2 Convective Stability of Polytropes

If we begin with the First Law of Thermodynamics,

$$TdS = dE + PdV \quad (3)$$

and use EOS MR, together with some of the relations derived in Appendix B, we can put this in the form

$$TdS = f(s, n)dP/\rho \quad (4)$$

The star will be stable if $dS/dP < 0$ throughout the star, recalling that $dP/dr < 0$. Applying this we find that the condition for local convective stability is

$$\frac{n_{crit}}{n_{crit} + 1} > \frac{(1 + s_r)(3/2 + 12s_r)}{(1 + 4s_r)^2 + 3/2 + 12s_r} \quad (5)$$

Where we have used $s_r = s(r) = P_{rad}(r)/P_{matter}(r)$ to distinguish between this function of r and the constant parameter s_c . To utilize this local condition to find out what stellar models are stable, we first must calculate how s_r varies through the star. Carrying out this calculation yields

$$s_r(1 + s_r)^4 \propto \frac{P^3}{\rho^4} \propto P^{\frac{3-n}{1+n}} \quad (6)$$

- We see that, for $n < 3$, the largest value of s_r is $s_c = s_r(r = 0)$, so the largest value of $n_{crit}(s_r)$ is $n_{crit}(s_c)$ and therefore if $n > n_{crit}(s_c)$, the star is stable.

- Since $n_{crit}(s_r) \geq 3/2$, no polytrope with $n < 3/2$ can be stable.

- For $3/2 < n < 3$, there is a maximum value of s_c for which the star is stable, determined from $n = n_{crit}(s_c)$, which rises from $s_c = 0$ at $n = 3/2$ to $s_c \rightarrow \infty$ for $n = 3$. For instance, at $n = 2.0$, $s_c^{MAX} = 0.3$; for $n = 2.5$, $s_c^{MAX} = 1.674$ (see Tab. 1 and Fig. 1)

- For $n = 3$, s_r is constant, and $n_{crit}(s_r) < 3$ for any finite s_r , so all models are stable.

- Since, for $n > 3$, $s_r \rightarrow \infty$ at the star's edge (where $P \rightarrow 0$), so the largest value of $n_{crit}(s_r) \equiv 3$ for any choice of s_c . Thus, all models with finite s_c are stable.

It is important to emphasize that the convective-stability condition described here is not an absolute stability criterion. Stars outside of this mass range certainly can exist, simply containing convection zones. The instability of these models arises because of our insistence on an exact polytropic pressure-density relation ($P = \kappa\rho^\Gamma$) and our use of

Table 1. Summary of the parameters describing the models we have studied, where $\tilde{m} = M_{star}/M_{scale}$.

| n | \tilde{m} | s_c |
|-----|-------------|--------|
| 2.0 | 10 | 0.0256 |
| 2.5 | “ | 0.0227 |
| 3.0 | “ | 0.0181 |
| 4.0 | “ | 0.0117 |
| 2.5 | 100 | 0.5965 |
| 3.0 | “ | 0.5515 |
| 4.0 | “ | 0.4219 |
| 3.0 | 1000 | 2.995 |
| 4.0 | “ | 2.600 |

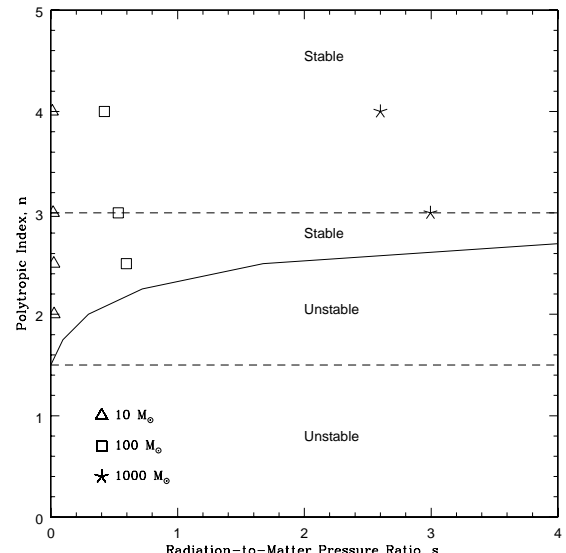


Figure 1. A plot summarizing the results of the stability analysis described in §4.2. Convectively stable and unstable regions of the polytropic index / s_c parameter space are labeled, and the models we have selected from this parameter space are marked.

EOS MR. Since our goal was not to be exhaustive, but to elucidate what differences among the explosions of stars with a variety of density profiles – from the highly centrally-condensed $n = 4$ stars to the diffuse $n = 2$ models – complicating our study with convective stars was unnecessary.

4.3 Description of analysis

The chief way in which we shall summarize the results of an explosion is in terms of the mass ejected as a function of explosion energy. We begin by discussing how we derive the ejected mass from the numerical simulations. For EOS M (no radiation pressure), the code was run until the remnant core had become stationary and had nearly re-assumed hydrostatic equilibrium, i.e., it had local gas velocities near zero ($< 10^{-7} R_{stellar}/\text{dynamical time}$) and satisfied the virial theorem. The mass loss was determined by finding the location in the outermost Lagrangian grid of the zone for which the local energy (sum of kinetic, thermal and gravitational contributions) density changed from negative

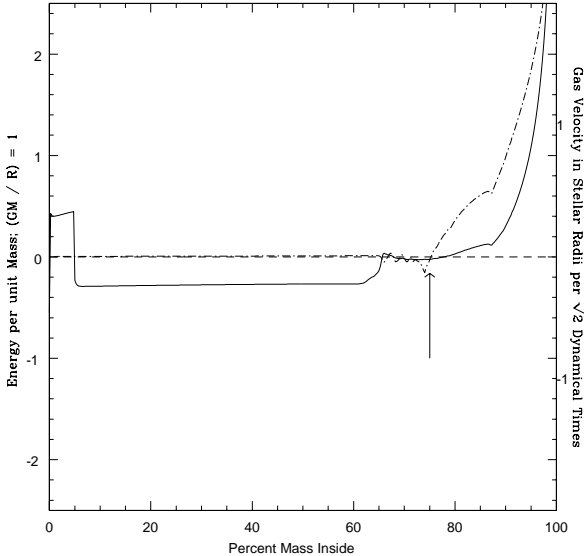


Figure 2. The asymptotic local energy density (solid line) for $n = 3$ polytrope (no radiation pressure) and $E_{blast} = E_{bind}$ after the central core has reattained hydrostatic equilibrium, in units for which $(GM/R) = 1$. The dash-dotted line gives the local velocity, in units of stellar radii per $\sqrt{2}$ dynamical times. The dashed line is a reference line for zero energy and velocity.

to positive. A graph of the local energy density for a typical star after an explosion is included as Fig. 2.

A drawback of this method is apparent in Fig. 1. Though there are distinct portions of the star that can definitely be said to be either remnant or ejecta, there is also a small region with nearly zero energy, resembling an atmosphere around the remnant. These atmospheres did not appear in all explosions – typically, they occurred when $E_{blast} \sim 0.7 - 1.0 E_{bind}$ – and when they did, the code was simply run long enough for a reasonably clear separation to be determined.

When our previous method for determining the amount of mass loss gave ambiguous results, we moved to a different method for deciding which mass shells were ejecta and which were remnants. We stored the location and local energy density of each grid zone throughout the run. We plotted the location of the mass element as a function of time, using the sign of the local energy density to color code the lines. During the atmospheric motions some layers do work on other layers; the color coding shows changes from bound to unbound (and visa-versa). These plots proved to be helpful, illuminating the transient identities of bound atmospheres, marginally bound gas, and low energy ejecta. We adopted the following criterion for ending the calculation: we ceased when all outer shells had positive energy density and the number of intermediate shells with local energy density of changing sign was small – less than a couple of percent of the total mass. An example is shown in Fig. 3, where the apparent bifurcation point between bound and unbound material is marked on the far right. We determined in this case that by the time the code was stopped, the amount of thermal energy remaining in the outer region of the remnant was insufficient to eject many more mass shells, which is ap-

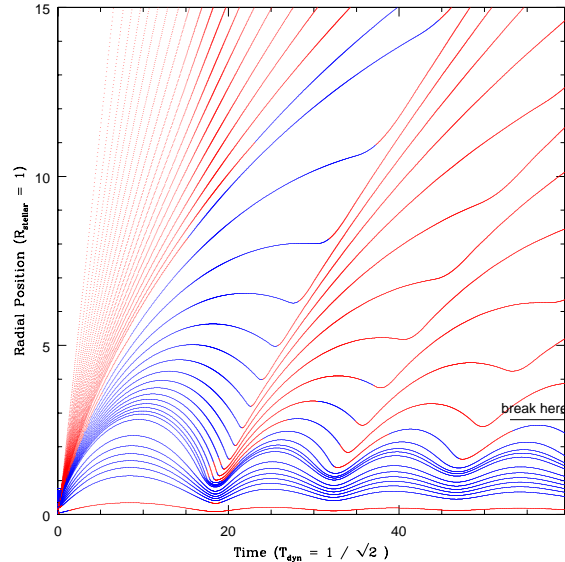


Figure 3. A typical graph of the motion of grid zones in time for an exploding star, in this case an $m = 100$ polytrope of index $n = 3$ with an explosion energy of 90 per cent of the star's binding energy. Each line tracks a representative mass shell. The Lagrangian mass intervals vary: lines in the ejected region and outer parts of the remnant – which represent escaping mass (large radii) and uppermost parts of the cooling, bouncing remnant (the blue lines) – are intervals of 0.5 – 1 per cent of the total mass. In the inner part of the remnant, each line represents approximately 10 per cent of the total mass. Where lines are red, the local energy density is positive; where blue, negative. The bifurcation point separating the remnant from the ejecta is marked. Radial distances are given in units of the initial stellar radius; times are given in units equal to $\sqrt{2}$ dynamical times.

parent from the diminishing amount of mass ejected with each stellar oscillation. We are confident of this prediction because it has been borne out in all cases where the code was run much longer, and, hence, closer to the point of the remnant's return to hydrodynamic stability. These plots also showed two distinct ways in which shells are ejected: 1) For $E_{bind}/E_{blast} > 0.5$ a small number of shells are lost in the initial explosion shock wave; these gain tremendous kinetic energies. The first 8 lines in this plot represent ~ 4 per cent of the mass; 3-7 per cent of the mass is lost in this way for this energy range. 2) The rest of the ejecta are expelled by the ringing down of the remnant.

Given our algorithm for the determination of mass loss in an explosion, we next investigated the extreme limits: total disruption explosions and failed explosions (no ejected mass). Total disruptions were relatively easy to recognize when all grid zones acquired positive energy in the first pass of the shock wave from the explosion. For explosion energies near the threshold for total stellar disruption, however, we found that there was typically a range of energies where a large portion of the stellar envelope was ejected, while leaving an extended remnant undergoing very slow, long-scale oscillations. The precise mass loss in most of these cases was impossible to determine, though it was always ~ 50 per cent. The artificial viscosity eventually damps these oscillations, but it takes a long time to do so. Total disruption

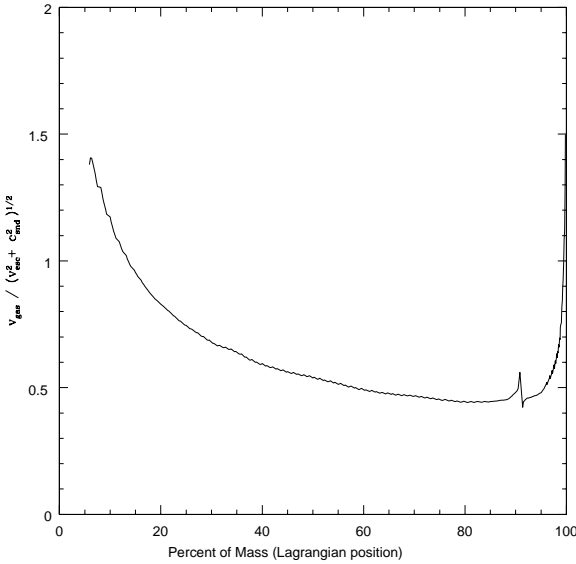


Figure 4. A plot of the $v_{\text{gas}} / \sqrt{v_{\text{esc}}^2 + c_{\text{snd}}^2}$, in this case for a star with $n = 1.5$, $s_c = 0.1$, and an explosion energy equal to 15 per cent of the star’s binding energy. The choppiness in the plot is due to non-physical effects in the determination of the exact location of the shock. Note the deceleration through the bulk of the star, with only the very outermost shells reaching escape velocity as the shock accelerates in the falling density profile near the edge.

happens abruptly, with every star studied going from the ~ 50 per cent mass loss oscillatory state to 100 per cent mass loss with only a small addition of explosion energy. We were able to pin down the width of the transition from remnant to total disruption as function of explosion energy to $\sim 5 - 10$ per cent in the star’s binding energy.

The failed explosion regime was computationally easier to study. Failed explosions produced no outgoing shells with positive energy. The results can be understood in terms of the speed of the shock as it proceeded through the star. Strong shocks slowed as they plowed through the dense core of the star, then accelerated when they reached the diffuse outer regions of the polytropes. In failed explosions the shock velocity fell below the sound speed in the middle region and/or failed to accelerate up to the local escape speed in the outer region. A plot of the process is included in Fig. 4. In the figure, we plot $v_{\text{shock}} / \sqrt{v_{\text{esc}}^2 + c_{\text{snd}}^2}$ – where v_{esc} is the escape velocity for the initial star and c_{snd} is the local sound speed – illustrating the falling shock Mach number in the core and the reacceleration to velocities allowing escape by the outer density gradient.

4.4 Explosions without radiation pressure

For the first round of explosions, we used EOS M (no radiation pressure). For these calculations, the solutions independent parameters are $E_{\text{blast}}/E_{\text{bind}}$ and the star’s polytropic index Γ .

We have included two figures summarizing the mass loss results. In the first, Fig. 5, the explosions are compared with each other, showing great similarity among the models. In Fig. 6, we have separated each polytrope into its own win-

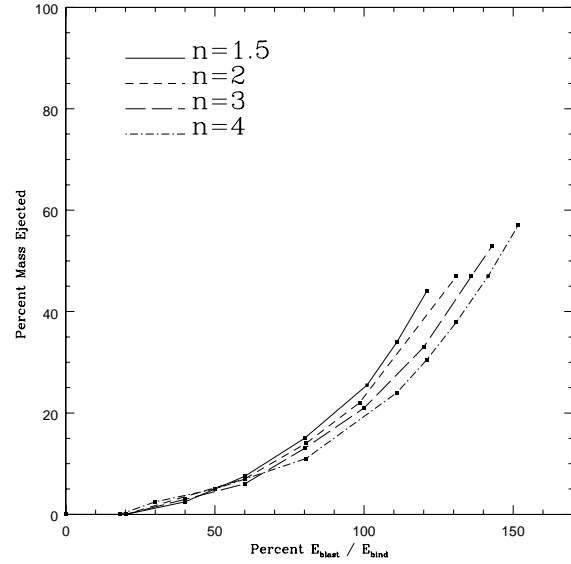


Figure 5. This figure summarizes the mass loss percentages resulting from explosions in polytropes of four different indices without radiation.

dow to compare its mass loss curve to a couple of “rules of thumb” Fryer & Kalogera (2001). The first line, the dash-dotted curve, is the simplest such rule. It represents the mass loss if 100 per cent of the explosion energy were distributed in such a way as to give as many of the outer shells of the star exactly escape velocity, while leaving untouched those parts of the star which remain bound. This is, of course, physically impossible, but it does provide an upper bound on mass loss. The dashed curve represents the actual choice made by Fryer & Kalogera (2001), which essentially splits the explosion energy budget in two, giving 50 per cent to unbind the star directly, and 50 per cent to heat the remnant and to accelerating the ejecta. This version gives results that are much closer to our numerical calculation, but *overestimates mass loss in low energy explosions* and also *overestimates the amount of energy required to completely unbind the star*.

4.5 Explosions with radiation pressure

For the second round of explosions, we used the hydrodynamics code with EOS MR (matter and radiation pressure). The parameter space now included three variables: explosion energy, polytropic index, and M_{star} . We chose three stellar masses, $\tilde{m} = 10, 100$, and 1000 , and then surveyed the range of polytropic indices for which stars of these masses were convectively stable. For each star, we varied explosion energy from cases of failed explosions to total stellar disruption. The results of these explosions are summarized in Figs. 7, 8, and 9. Because of the difficulty of precisely determining the line of bifurcation between remnant and ejecta, error bars representing the range of the star where the bifurcation point may occur have been included. This range of uncertainty was determined by finding the region of the star for which the final computed velocity and local energy density were not in agreement; that is, zones that have nega-

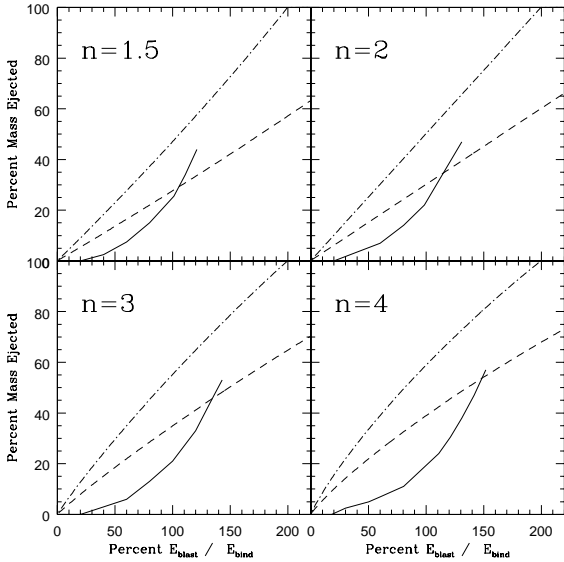


Figure 6. Mass loss curves are compared with two simple assumptions relating explosion energy and mass loss. The steeper, dashed curve represents the most efficient possible application of the explosion energy to mass loss. The second, dash-dotted curve represents the more physically reasonable assumption that 50 per cent of the energy goes into unbinding part of the star, and 50 per cent goes into both heating the remaining star and to net kinetic energy for the ejecta.

tive local energy density, but are moving outward at several stellar radii, or infalling zones with positive local energy density are considered to have ambiguous fates. The number of these zones is always small, however, at the most comprising a couple of percent of the stellar mass.

Note that in all these cases, the mass-loss curves are remarkably uniform, especially given the variation in binding energy among the stellar models explored here (more details on binding energy given in the Appendix). The uniformity in the shapes of the mass-loss curves found here allows them to be described accurately by a fitting formula. The form that best fits the data is

$$\frac{M_{\text{lost}}}{M_{\text{star}}} = \begin{cases} 0 & e < e_o \\ A(e_{\text{blast}} - e_0)^2 & e_o < e < e_f \\ 100 & e_f < e \end{cases} \quad (7)$$

where e_{blast} (e_o , e_f) is blast energy (minimum blast energy to cause mass loss, maximum blast energy to leave a bound core) measured as a percent of binding energy (i.e. $e_{\text{blast}} = 100 \times E_{\text{blast}}/E_{\text{bind}}$, etc.) and A is the fitting parameter. A sample comparison between the fits and the numerical data is shown graphically in Fig. 10; the parameters describing each explosion's fit are contained in Table 2.

Notice that in all cases, total disruption occurs near or slightly above the original stellar binding energy, i.e. at $E_{\text{blast}} > e_f E_{\text{bind}}$ with $e_f \geq 100$ per cent generally. The transition to total disruption is also very abrupt. Just below e_f , the amount of mass lost is below 50 per cent in all cases.

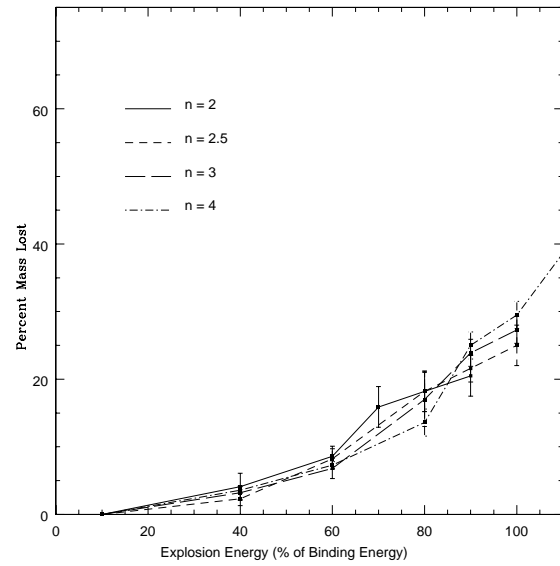


Figure 7. This figure summarizes the mass loss percentages for explosions in $\tilde{m} = 10$ stars. Error bars represent the uncertainty in the determination of the remnant - ejecta bifurcation point.

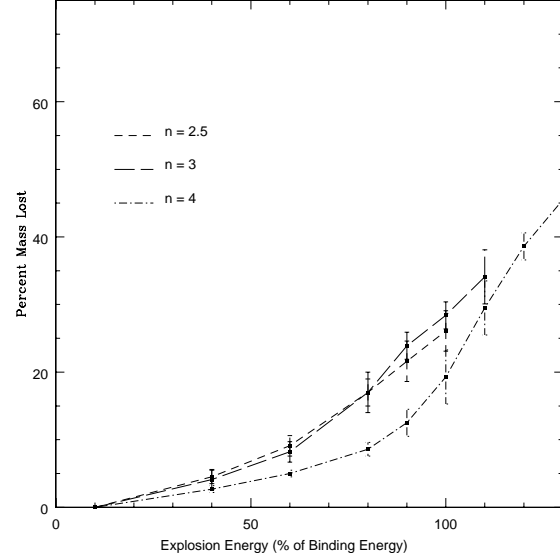


Figure 8. This figure summarizes the mass loss percentages for explosions in $\tilde{m} = 100$ stars. Error bars represent the uncertainty in the determination of the remnant - ejecta bifurcation point.

5 OTHER INNER BOUNDARY CONDITIONS

Next, we investigate the influence of adding a compact core at the center of our simulation. For our first test, we left the explosion set-up the same, but changed our treatment of the inner regions of the star. At one extreme, we took the innermost zone to be a hard, reflecting sphere; at the other extreme, we fixed an arbitrary spatial radius within which all gas would be pressure-free (that is to say, any zone starting inside that radius, or falling back inside it became pressure free immediately). The hard sphere inner core might repre-

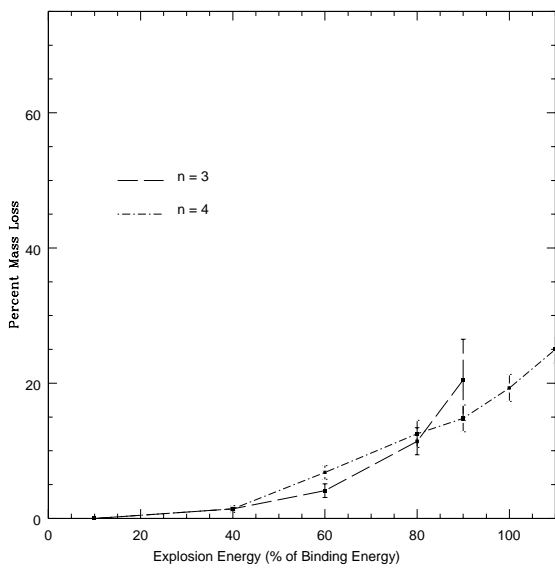


Figure 9. This figure summarizes the mass loss percentages for explosions in $\tilde{m} = 1000$ stars. Error bars represent the uncertainty in the determination of the remnant - ejecta bifurcation point.

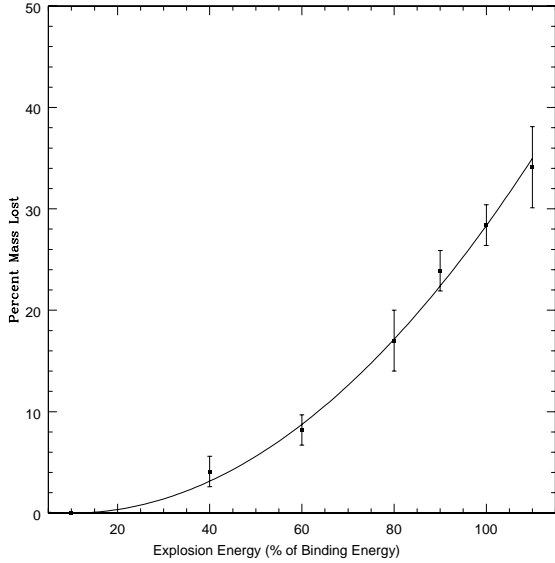


Figure 10. A figure comparing the results of the fitting formula, Eqn. 7, to the data, in this case for an $n = 3$, $\tilde{m} = 100$ star.

sent a neutron star, whereas the pressure-free infall at inner radii might mimic highly supersonic, irreversible infall into a ‘vacuum cleaner’ black hole. We ran several cases – polytropes of indices between 1.5 and 4, with a variety of values of s_c (and thus M_{star}), with the arbitrary inner ‘vacuum cleaner’ radius varying between 2 and 30 per cent of the mass (in Lagrangian coordinates).

The mass loss computed with these boundary conditions differed little from what was found in our earlier survey with an adiabatically expanding core, with changes that were unnoticeable even when quite a large inner region – as

Table 2. Summary of fitting parameters for various explosion scenarios. $e_o = 100 \times E_o/E_{\text{bind}}$, $e_f = 100 \times E_f/E_{\text{bind}}$

| n | \tilde{m} | $A(\times 10^{-3})$ | e_o | e_f |
|-----|-------------|---------------------|-------|-------|
| 2.0 | 10 | 3.57 | 10 | 110 |
| 2.5 | “ | 3.37 | 11 | 120 |
| 3.0 | “ | 3.47 | 10 | 120 |
| 4.0 | “ | 3.67 | 10 | 130 |
| 2.5 | 100 | 2.89 | 5 | 120 |
| 3.0 | “ | 3.50 | 10 | 130 |
| 4.0 | “ | 2.95 | 11 | 140 |
| 3.0 | 1000 | 3.74 | 20 | 110 |
| 4.0 | “ | 2.44 | 10 | 130 |

much as 15 - 20 per cent, in mass – of the star was allowed to become pressure-free. Intuitively, this insensitivity seems linked to the physics of the 50 per cent mass loss bifurcation. In those cases that remain bound, it is the trading of energy among the outer shells that determines the amount of mass lost, while the inner half of the star, which is sensitive to the treatment of the inner zones, is never in danger of being lost. In stars that are totally dispersed, the explosion is so violent that differences in the inner boundary conditions have little effect, since no portion of the star ever falls back to experience them.

6 CONCLUSION

Here, we have confined ourselves to a rather idealized and simplified problem, partially disruptive explosions of progenitors whose density profiles are solutions to the Lane-Emden equation, but with varying ratios of radiation to matter pressure. In this way, we have been able to survey models in a well-defined parameter space fairly extensively, trading the concreteness of real stellar models for the flexibility of parametrized ideal models. Specifically, we have determined the fraction of the original stellar mass ejected as a function of explosion energy in polytropes of index $n = 1.5$, 2, 3, and 4 in calculations without radiation pressure; we also explored the mass loss fractions for stars of $\tilde{m} = 10$, 100, and 1000 over a range of n from 2.0 to 4.0. Our results suggest that the mass loss is remarkably uniform, even among widely varying stellar density profiles and over an enormous range in stellar masses. We have provided a simple, parametrized formula for the fractional mass loss as a function of explosion energy for a range of values of n and the ratio of radiation to matter pressures; see Eq. (7) and Table 2.

One striking feature of all the models we tested was that the mass loss fraction as a function of explosion energy appears to be discontinuous at around 50 per cent mass loss, with a small (few per cent) difference in explosion energy separating stars which lose half their mass from totally disrupted stars. Because our simulations did not include formation of a compact remnant at the centre, this result cannot be taken as a concrete demonstration that the observation of a black hole of mass M demands a progenitor whose mass was less than about twice as large.

The abrupt transition between moderate (i.e. $\lesssim 50$ per cent) and almost total disruption found here for wide classes of initial models is also seen in modelling of explosions in sets

of specific progenitors (e.g. Woosley & Weaver 1995, Table 3; MacFadyen et al. 2001, Table 1). Thus, we conjecture that even when a compact central remnant is included, the results divide into two separate cases depending on whether the explosion energy is above or below, approximately, the critical value found here for complete disruption. It is significant that this bifurcation effect appears, as it does in our simulation, at the most basic, hydrodynamic level, implying that its appearance in more sophisticated models rests chiefly on these underlying physics. For explosion energies below this critical value, there is a sharp transition between modest (i.e. $\lesssim 50$ per cent) mass loss and total disruption apart from the compact remnant. For explosion energies above the cutoff, either a black hole or neutron star may form. However, in this case, we expect much smaller fallback masses, generally only a few tenths of M_\odot or less, primarily caused by reverse shock propagation through the core, and the consequent deceleration of a small amount of outgoing matter (e.g. Woosley 1988; Chevalier 1989).

Supernovae frequently occur in binary systems. In such systems, when there are very energetic explosions and little mass fallback, we expect little mass contamination of the atmosphere of the binary companion. The outgoing regions of the progenitor intercepted by the companion are not captured; indeed the outer layers of the companion are stripped and ablated by the ejecta. On the other hand, when the explosion is weak and substantial mass fallback occurs, progenitor material may fall back onto the companion, polluting its atmosphere. In the latter cases, we would then infer that a remnant of mass M was most likely derived from a progenitor with mass less than $\simeq 2M$. Thus, in systems like Nova Scorpii that show evidence for black hole formation in a supernova (e.g. Israeli et al. 1999), we conjecture that mass of the pre-explosion star was, in fact, less than twice the present mass inferred for the black hole remnant (which also has accreted matter since forming, presumably). This may have implications for the dynamics of such systems (e.g. Mirabel et al. 2002). We caution, though, that our results may be altered somewhat in more refined models. Further studies are underway to include a compact central remnant, density jumps (expected as a consequence of compositional inhomogeneity), rotation and explosion asymmetries. These new calculations will continue, in the same spirit as those reported here, to employ the simplest explosion models needed to reveal the underlying physical consequences of the various refinements, and to allow a survey of the hydrodynamics of a large range of explosion models.

ACKNOWLEDGMENTS

This research was supported in part by NASA-ATP grant NAG5-8356. M.W. is supported by an NSF Graduate Fellowship. I.W. acknowledges the hospitality of KITP, which is supported by NSF grant PHY99-07949, where part of this research was carried out, as well as support from NSF Grant AST-0307273 and from IGPP at LANL.

REFERENCES

Chevalier, R. A. 1989, ApJ, 346, 847.

Fryer, C. L. & Kalogera, V. 2001, ApJ, 554, 548

Israeli, G., Rebolo, R., & Basri, G., 1999, Nat, 401, 142

Landau, L. D., and Lifshitz, E. M. 1987, Fluid Mechanics, Pergamon Press: Oxford

MacFadyen, A. I., Woosley, S. E., & Heger, A., 1999, ApJ, 524, 262

MacFadyen, A. I., Woosley, S. E. and Heger, A. 2001, ApJ, 550, 410.

Mirabel, I. F., Mignani, R., Rodrigues, I., Combi, J. A., Rodríguez, & L. F., Guglielmetti, F. 2002, A&A, 395, 595

Nadezhin, D. K. and Frank-Kamenetskii, D. A. 1963, Soviet Astronomy, 6, 779

Orosz, J. & Bailyn, C. 1997, ApJ, 477, 876

Richtmyer, R. & Morton, K. W. 1967, Difference Methods For Initial-Value Problems, John Wiley & Sons: New York

Shahbaz, T., van der Hooft, F., Casares, J., Charles, P. A., & van Paradijs, J. 1999, MNRAS, 306, 89

Woosley, S. E. 1988, ApJ, 330, 281.

Woosley, S. E. and Weaver, T. A. 1995, ApJS, 101, 181.

APPENDIX A: DIFFERENCE EQUATIONS

The Lax-Wendroff difference equations for the equations of hydrodynamics in one dimension with spherical symmetry are as follows. Note that the pressure in the equation for advancing energy must be solved for using the equation of state to make this set of difference equations explicit rather than implicit. In the difference equations, n represents time steps, while j represents spatial steps. The equations are non-dimensionalized simply, with each variable scaled to order unity for the initial conditions in all calculations we have done. The one remaining constant, ρ_o , with units of density, sets the overall scale of the system studied. The variable R records the position of each shell. Comparing each shell's current position, R , with r , a static, reference grid, allows the gas's local density to be calculated. The remaining variables are interdependent. The equation for moving grid zones is:

$$\frac{R_j^{n+1} - R_j^n}{\Delta t} = u_j^{n+1}. \quad (A1)$$

The conservation of momentum equation is:

$$\frac{u_j^{n+1} - u_j^n}{\Delta t} = -\frac{1}{\rho_o} \frac{(\delta p)_j^n}{\Delta r} \left(\frac{R_j^n}{r_j} \right)^2. \quad (A2)$$

The conservation of mass equation is:

$$\rho_{j+1/2}^{n+1} = \rho_o \frac{(r_{j+1})^3 - (r_j)^3}{(R_{j+1}^{n+1})^3 - (R_j^{n+1})^3}. \quad (A3)$$

The First Law of Thermodynamics is:

$$U_{j+1/2}^{n+1} = U_{j+1/2}^n - \left(\frac{p_{j+1/2}^{n+1} + p_{j+1/2}^n}{2} \right) \times \left(\frac{1}{\rho_{j+1/2}^{n+1}} - \frac{1}{\rho_{j+1/2}^n} \right). \quad (A4)$$

Where U = internal energy / mass. The acceleration of the innermost shell is determined by treating its volume as filled with a gas of uniform pressure so that the shell's equation

of motion is:

$$\begin{aligned} m_{inner} \frac{\partial v}{\partial t} &= 4\pi(p_{inner} - p_{outer}) \Rightarrow \\ u_0^{n+1} &= u_0^n + 4\pi\Delta t(p_{inner} - p_{outer}). \end{aligned} \quad (\text{A5})$$

The pressure within the inner sphere varies adiabatically as the shell moves, i.e.,

$$p_{inner}(t) = p_o \left(\frac{V_o}{V(t)} \right)^\gamma. \quad (\text{A6})$$

These equations are completed by some equation of state,

$$p_{j+1/2}^{n+1} = f(U_{j+1/2}^{n+1}, \rho_{j+1/2}^{n+1}). \quad (\text{A7})$$

If this equation of state can be algebraically solved, the full set of equations is explicit; if it cannot be solved, then an implicit step and numerical root-finding procedure is required to advance the grid. The advancement of the grid proceeds as follows. 1) Using the conservation of momentum, the new gas velocities are set throughout the system. 2) Boundary conditions are applied. 3) The shell position, R , is advanced according to the new gas velocities. 4) R is then used to set the density throughout the system. 5) Two possibilities: if the equation of state is explicitly soluble, then the internal energy of the gas is determined. If not, then the pressure and energy equations must be stated in terms of the temperature and then solved, together with the First Law, numerically – three equations for three variables, p , U , and T . The above prescription must be modified slightly to accommodate shock fitting. To this end, we introduce an artificial viscous pressure, q , given by the differenced form,

$$q_{j+1/2}^n = \begin{cases} \frac{2a^2[(\delta u)_{j+1/2}^n]^2}{1/\rho_{j+1/2}^n + 1/\rho_{j+1/2}^{n-1}} & \text{if } (\delta u)_{j+1/2}^n < 0 \\ 0 & \text{if } (\delta u)_{j+1/2}^n \geq 0 \end{cases} \quad (\text{A8})$$

Note the parameter, a , which controls how widely the viscous pressure spreads the shock. Optimal values are $1.5 < a < 2.0$, which spread the shock over 3-10 zones. This artificial viscous pressure is added to the regular gas pressure in the above equations as follows: In the conservation of momentum equation,

$$(\delta p)_j^n \rightarrow (\delta p)_j^n + (\delta q)_j^n \quad (\text{A9})$$

and in the energy conservation equation,

$$\frac{p_{j+1/2}^{n+1} + p_{j+1/2}^n}{2} \rightarrow \frac{p_{j+1/2}^{n+1} + p_{j+1/2}^n}{2} + q_{j+1/2}^{n+1}. \quad (\text{A10})$$

When advancing the grid with artificial viscous pressure, the artificial viscosity term, q , is advanced before the energy equation, step 5 in the previous description.

APPENDIX B: SETTING UP MASS SHELLS IN A POLYTROPE

In the initial configuration whose mass and radius are M_* and R_* , define a mass coordinate $\hat{m} = M/M_*$ so that the shell is at radius $\hat{r}(\hat{m}) = R(M)/R_*$.

Let the pressure and density be $P(M) = \hat{P}(\hat{m})(GM_*^2/R_*^4)$ and $\rho(M) = \hat{\rho}(\hat{m})M_*/R_*^3$, respectively. At the center of the star, we can find $\hat{P}(0) = f_P(n)$ and $\hat{\rho}(0) = f_\rho(n)$, where n is the polytropic index. At

any other point in the star, we have $\rho(M) = \rho(0)\theta^n$ and $P(M) = P(0)\theta^{n+1}$. Thus, we have

$$\hat{P}(\hat{m}) = f_P(n)[\theta(\hat{m})]^{n+1} \quad \hat{\rho}(\hat{m}) = f_\rho(n)[\theta(\hat{m})]^n. \quad (\text{B1})$$

Usually, we specify the Lane-Emden function as a function of a dimensionless radius. Getting $\hat{r}(\hat{m})$ then requires a little bit of work. The method is this: the mass inside a physical radius R is

$$M(R) = 4\pi \int_0^R dr r^2 \rho(r) = 4\pi r_{\text{scale}}^3 \int_0^x dx x^2 [\theta(x)]^n, \quad (\text{B2})$$

where r_{scale} is the radius scale. Divide by the total mass to get the conversion equation

$$\hat{m} = \frac{\int_0^x dx x^2 [\theta(x)]^n}{\int_0^{x_0(n)} dx x^2 [\theta(x)]^n} = \frac{\int_0^{x_0(n)\hat{r}(\hat{m})} dx x^2 [\theta(x)]^n}{\int_0^{x_0(n)} dx x^2 [\theta(x)]^n}, \quad (\text{B3})$$

where $\theta(x_0(n)) = 0$ and we have used the fact that the scaled Lane-Emden radius variable $x = x_0(n)\hat{r}(\hat{m})$. This equation can be inverted numerically to get $\hat{r}(\hat{m})$, and we can use the result to evaluate the pressure and density:

$$\begin{aligned} \hat{P}(\hat{m}) &= f_P(n)[\theta(x_0(n)\hat{r}(\hat{m}))]^{n+1} \\ \hat{\rho}(\hat{m}) &= f_\rho(n)[\theta(x_0(n)\hat{r}(\hat{m}))]^n. \end{aligned}$$

We are interested in polytropic models where the pressure is supplied by a mixture of radiation and a nonrelativistic gas. The total pressure in physical units is then

$$P = \frac{\rho k T}{\mu} + \frac{1}{3}aT^4 = P_{\text{gas}} + P_{\text{radiation}}, \quad (\text{B4})$$

where μ is the mass per nonrelativistic particle in the star. We define s

$$s = \frac{P_{\text{radiation}}}{P_{\text{gas}}} = \frac{aT^3\mu}{3\rho k}, \quad (\text{B5})$$

which varies throughout the star. At any point in the star, we can use this to eliminate temperature in favor of s :

$$\begin{aligned} T &= \left(\frac{3\rho sk}{a\mu} \right)^{1/3} \Rightarrow \\ P &= \frac{\rho k T (1+s)}{\mu} = \left(\frac{\rho k}{\mu} \right)^{4/3} \left(\frac{3s}{a} \right)^{1/3} (1+s). \end{aligned}$$

From this it follows that

$$\begin{aligned} \frac{P}{P(0)} &= \left(\frac{\rho}{\rho(0)} \right)^{1+1/n} = [\theta((x_0(n)\hat{r}(\hat{m})))]^{n+1} \\ &= \left(\frac{\rho}{\rho(0)} \right)^{4/3} \left(\frac{s}{s(0)} \right)^{1/3} \left(\frac{1+s}{1+s(0)} \right) \\ &= [\theta((x_0(n)\hat{r}(\hat{m})))]^{4n/3} \left(\frac{s}{s(0)} \right)^{1/3} \left(\frac{1+s}{1+s(0)} \right), \end{aligned}$$

We can use this to solve for $s(\hat{m})$ via

$$[s(\hat{m})]^{1/3}[1+s(\hat{m})] = [s(0)]^{1/3}[1+s(0)][\theta(x_0(n)\hat{r}(\hat{m}))]^{1-n/3}.$$

The thermal or internal energy density inside the star is, in physical units,

$$\begin{aligned} \rho U &= \frac{3\rho k T}{2\mu} + aT^4 = \frac{3\rho k T}{2\mu}(1+2s) \\ &= \frac{3}{2} \left(\frac{\rho k}{\mu} \right)^{4/3} \left(\frac{3s}{a} \right)^{1/3} (1+2s); \end{aligned} \quad (\text{B6})$$

compare this with the pressure

$$P = \left(\frac{\rho k}{\mu}\right)^{4/3} \left(\frac{3s}{a}\right)^{1/3} (1+s) . \quad (\text{B7})$$

Define $\gamma(\hat{m})$ by $P = (\gamma(\hat{m}) - 1)\rho U$, to find that

$$\frac{\rho U}{P} = (\gamma(\hat{m}) - 1)^{-1} = \frac{3}{2} \left[\frac{1+2s(\hat{m})}{1+s(\hat{m})} \right] ; \quad (\text{B8})$$

let $U = (GM_*/R_*)\hat{U}$ to find that

$$\hat{U}(\hat{m}) = \frac{3f_P(n)}{2f_\rho(n)} \theta(x_0(n)\hat{r}(\hat{m})) \left[\frac{1+2s(\hat{m})}{1+s(\hat{m})} \right] . \quad (\text{B9})$$

This completes the setup of the initial conditions of the polytrope.

We will also need to have the total energy of the star because we want to choose the blast energy as a fraction of the binding energy. The gravitational energy of a polytrope of index n is

$$E_{\text{grav}} = -\frac{3GM_*^2}{(5-n)R_*} . \quad (\text{B10})$$

The internal energy of the star is

$$\begin{aligned} E_{\text{int}} &= 4\pi \int_0^{R_*} dr r^2 \rho(r)U(r) = \int_0^{M_*} dM U(M) \\ &= \frac{3f_P(n)GM_*^2}{2f_\rho(n)R_*} \int_0^1 d\hat{m} \theta(x_0(n)\hat{r}(\hat{m})) \left[\frac{1+2s(\hat{m})}{1+s(\hat{m})} \right] . \end{aligned}$$

This is enough to get the total energy, but we can be a slight bit more elegant by using the virial theorem,

$$\begin{aligned} -E_{\text{grav}} &= 3 \int dM \frac{P}{\rho} \\ &= \frac{3f_P(n)GM_*^2}{f_\rho(n)R_*} \int_0^1 d\hat{m} \theta(x_0(n)\hat{r}(\hat{m})) , \quad (\text{B11}) \end{aligned}$$

from which we find that

$$\begin{aligned} E_{\text{tot}} &= -\frac{3GM_*^2}{2(5-n)R_*} \times \\ &\quad \left[\frac{\int_0^1 d\hat{m} \theta(x_0(n)\hat{r}(\hat{m}))[1+s(\hat{m})]^{-1}}{\int_0^1 d\hat{m} \theta(x_0(n)\hat{r}(\hat{m}))} \right] . \quad (\text{B12}) \end{aligned}$$

If we define $E_{\text{tot}} = -\hat{E}_{\text{tot}}[3GM_*^2/2(5-n)R_*]$ we see that

$$\hat{E}_{\text{tot}} = \frac{\int_0^1 d\hat{m} \theta(x_0(n)\hat{r}(\hat{m}))[1+s(\hat{m})]^{-1}}{\int_0^1 d\hat{m} \theta(x_0(n)\hat{r}(\hat{m}))} \quad (\text{B13})$$

$$= \frac{\int_0^1 d\hat{m} \frac{\hat{P}(\hat{m})}{\hat{\rho}(\hat{m})}[1+s(\hat{m})]^{-1}}{\int_0^1 d\hat{m} \frac{\hat{P}(\hat{m})}{\hat{\rho}(\hat{m})}} . \quad (\text{B14})$$

APPENDIX C: DYNAMICAL EQUATIONS

The equation of motion for a mass shell is

$$\frac{\partial^2 R(M, t)}{\partial t^2} = -4\pi R^2(M, t) \frac{\partial P(M, t)}{\partial M} - \frac{GM}{R^2(M, t)} + a_{\text{visc}}(M, t) , \quad (\text{C1})$$

where $a_{\text{visc}}(M, t)$ is the viscous acceleration (which we include using a prescribed artificial viscosity). Introducing our

nondimensional radius, pressure and mass implies

$$\begin{aligned} R_* \frac{\partial^2 \hat{r}(\hat{m}, t)}{\partial t^2} &= \frac{GM_*}{R_*^2} \left[-4\pi \hat{r}^2(\hat{m}, t) \frac{\partial \hat{P}(\hat{m}, t)}{\partial \hat{m}} - \frac{\hat{m}}{\hat{r}^2(\hat{m}, t)} \right] + a_{\text{visc}}(\hat{m}, t) ; \quad (\text{C2}) \end{aligned}$$

Define a dimensionless time by $t = (R_*^3/GM_*)^{1/2}\tau$; then

$$\begin{aligned} \frac{\partial^2 \hat{r}(\hat{m}, \tau)}{\partial \tau^2} &= -4\pi \hat{r}^2(\hat{m}, \tau) \frac{\partial \hat{P}(\hat{m}, \tau)}{\partial \hat{m}} \\ &\quad - \frac{\hat{m}}{\hat{r}^2(\hat{m}, \tau)} + \hat{a}_{\text{visc}}(\hat{m}, \tau) , \quad (\text{C3}) \end{aligned}$$

where the viscous acceleration is defined by $a_{\text{visc}}(M, t) = \hat{a}_{\text{visc}}(\hat{m}, \tau)(GM_*/R_*^2)$. Since we shall actually want equations that are first order in time, we note that the radial velocity is

$$\begin{aligned} \frac{\partial R(M, t)}{\partial t} &= \left(\frac{GM_*}{R_*}\right)^{1/2} \frac{\partial \hat{r}(\hat{m}, \tau)}{\partial \tau} \\ &= \left(\frac{GM_*}{R_*}\right)^{1/2} \hat{v}(\hat{m}, \tau) , \quad (\text{C4}) \end{aligned}$$

and therefore

$$\begin{aligned} \frac{\partial \hat{r}(\hat{m}, \tau)}{\partial \tau} &= \hat{v}(\hat{m}, \tau) \\ \frac{\partial \hat{v}(\hat{m}, \tau)}{\partial \tau} &= -4\pi \hat{r}^2(\hat{m}, \tau) \frac{\partial \hat{P}(\hat{m}, \tau)}{\partial \hat{m}} \\ &\quad - \frac{\hat{m}}{\hat{r}^2(\hat{m}, \tau)} + \hat{a}_{\text{visc}}(\hat{m}, \tau) . \quad (\text{C5}) \end{aligned}$$

From the first law of thermodynamics, we get that

$$\frac{\partial U(M, t)}{\partial t} = q_{\text{visc}}(M, t) - P(M, t) \frac{\partial}{\partial t} \left[\frac{1}{\rho(M, t)} \right] , \quad (\text{C6})$$

where $q_{\text{visc}}(M, t)$ is the viscous heating, which we take to be

$$q_{\text{visc}}(M, t) = \begin{cases} -a^2 \rho(M, t) \left(\frac{\partial v}{\partial R}\right)^2 \frac{\partial}{\partial t} \left[\frac{1}{\rho(M, t)} \right] & \text{if } \left(\frac{\partial v}{\partial R}\right) < 0 \\ 0 & \text{if } \left(\frac{\partial v}{\partial R}\right) \geq 0 \end{cases}$$

where a is a constant with units of length. Introducing the same nondimensional variables as in the polytrope setup we find that

$$\begin{aligned} \frac{\partial \hat{U}(\hat{m}, \tau)}{\partial \tau} &= - \left(a^2 \hat{\rho}(\hat{m}, \tau) \left(\frac{\partial \hat{v}}{\partial \hat{r}}\right)^2 + \hat{P}(\hat{m}, \tau) \right) \times \\ &\quad \frac{\partial}{\partial \tau} \left[\frac{1}{\hat{\rho}(\hat{m}, \tau)} \right] , \quad (\text{C7}) \end{aligned}$$

where the viscous heating is defined by $q_{\text{visc}} = \hat{q}_{\text{visc}}[(GM_*)^{3/2}/R_*^{5/2}]$. We can replace the pressure by

$$P = \frac{2\rho U}{3} \left(\frac{1+s}{1+2s} \right) \Rightarrow \hat{P} = \frac{2\hat{\rho}\hat{U}}{3} \left(\frac{1+s}{1+2s} \right) \quad (\text{C8})$$

to rewrite the first law in the form

$$\begin{aligned} \frac{\partial \hat{U}(\hat{m}, \tau)}{\partial \tau} &= \left(\frac{a^2}{\hat{\rho}(\hat{m}, \tau)} \left(\frac{\partial \hat{v}}{\partial \hat{r}}\right)^2 + \right. \\ &\quad \left. \frac{2\hat{U}(\hat{m}, \tau)[1+s(\hat{m}, \tau)]}{3\hat{\rho}(\hat{m}, \tau)[1+2s(\hat{m}, \tau)]} \right) \frac{\partial \hat{\rho}(\hat{m}, \tau)}{\partial \tau} . \quad (\text{C9}) \end{aligned}$$

We can close the loop using $U \propto \rho^{1/3}s^{1/3}(1+2s)$ to get

$$\frac{\hat{U}(\hat{m}, \tau)}{\hat{U}(\hat{m}, 0)} = \left(\frac{\hat{\rho}(\hat{m}, \tau)s(\hat{m}, \tau)}{\hat{\rho}(\hat{m}, 0)s(\hat{m}, 0)} \right)^{1/3} \left[\frac{1+2s(\hat{m}, \tau)}{1+2s(\hat{m}, 0)} \right] . \quad (\text{C10})$$

We could use this to find an equation for $s(\hat{m}, \tau)$ explicitly; then

$$\frac{\partial}{\partial \tau} \left[\frac{s(\hat{m}, \tau) e^{8s(\hat{m}, \tau)}}{\hat{\rho}(\hat{m}, \tau)} \right] = \left\{ \frac{3q_{\text{visc}}(\hat{m}, \tau)[1 + 2s(\hat{m}, \tau)]}{U(\hat{m}, \tau)} \right\} \times \frac{s(\hat{m}, \tau) e^{8s(\hat{m}, \tau)}}{\hat{\rho}(\hat{m}, \tau)}, \quad (\text{C11})$$

with $\hat{U}(\hat{m}, \tau)$ evaluated using Eq. (C10). Finally, the equation of mass conservation can be written as

$$\begin{aligned} \frac{1}{\rho(M, t)} &= 4\pi r^2(M, t) \frac{\partial r(M, t)}{\partial M} \Rightarrow \\ \frac{1}{\hat{\rho}(\hat{m}, \tau)} &= 4\pi \hat{r}^2(\hat{m}, \tau) \frac{\partial \hat{r}(\hat{m}, \tau)}{\partial \hat{m}}. \end{aligned} \quad (\text{C12})$$

If we wish, we can define a new variable $\hat{V}(\hat{m}, \tau) = 1/\hat{\rho}(\hat{m}, \tau)$, and rewrite the last few equations as

$$\begin{aligned} \hat{V}(\hat{m}, \tau) &= 4\pi \hat{r}^2(\hat{m}, \tau) \frac{\partial \hat{r}(\hat{m}, \tau)}{\partial \hat{m}} \\ \frac{\hat{U}(\hat{m}, \tau)}{\hat{U}(\hat{m}, 0)} &= \left[\frac{\hat{V}(\hat{m}, 0)s(\hat{m}, \tau)}{\hat{V}(\hat{m}, \tau)s(\hat{m}, 0)} \right]^{1/3} \left[\frac{1 + 2s(\hat{m}, \tau)}{1 + 2s(\hat{m}, 0)} \right] \\ \frac{\partial \hat{U}(\hat{m}, \tau)}{\partial \tau} &= - \left(\frac{a^2}{V(\hat{m}, \tau)} \left(\frac{\partial \hat{v}}{\partial \hat{r}} \right)^2 \right. \\ &\quad \left. + \frac{2\hat{U}(\hat{m}, \tau)[1 + s(\hat{m}, \tau)]}{3\hat{V}(\hat{m}, \tau)[1 + 2s(\hat{m}, \tau)]} \right) \frac{\partial \hat{V}(\hat{m}, \tau)}{\partial \tau} \end{aligned} \quad (\text{C13})$$

Eqs. (C5), and either Eqs. (C9), (C10) and (C12) or Eqs. (C13), with the initial conditions set up in the previous sections, can now be cast into finite difference form, with a suitable specification of the artificial viscous force and heating.

For all calculations done after the code was tested, we also included a Newtonian Gravitation force per unit mass via

$$F_{\text{grav}} = -\frac{GM(R)}{R^2}, \quad (\text{C14})$$

or in difference form,

$$F_j^n = -\frac{G\rho_o \frac{4\pi}{3} (r_j^n)^3}{(R_j^n)^2}. \quad (\text{C15})$$

This force was added to the conservation of momentum equation, the equation used to set gas velocities. Finally, the code self-checks by calculating total energy and momentum to ensure that these are conserved. For energy, the sum of the local energy in each zone is calculated first *via*

$$E_{\text{kinetic}} + E_{\text{therm}} = \sum_{i \in \text{zones}} \left(\frac{1}{2} u_i^2 + U_i \right) \Delta M_i. \quad (\text{C16})$$

The gravitational potential energy is then calculated via

$$E_{\text{grav}} = - \sum_{i \in \text{zones}} \frac{GM_{\text{enclosed}}}{R_i} \Delta M_i. \quad (\text{C17})$$

and the two energies are added and recorded as the current total energy in the system. Conservation of momentum is also checked though a simple summation:

$$P_{\text{tot}} = \sum_{i \in \text{zones}} u_{\text{zone}} \Delta M_i. \quad (\text{C18})$$

Finally, the algebraic equation used to determine the total local energy per unit mass of each zone – the quantity used to determine if a zone was bound or unbound – was

$$\begin{aligned} \frac{E_{\text{zone}=j}^{\text{tot}}}{\Delta M_j} &= \frac{E_j^{\text{therm}} + E_j^{\text{kinetic}} + E_j^{\text{potential}}}{\Delta M_j} \\ &= \frac{1}{2} u_j^2 + U_j - \frac{1}{2} \sum_{i=1}^{i \leq j} F_i^{\text{grav}} \Delta R_i, \end{aligned} \quad (\text{C19})$$

where $\Delta R_i = R_i - R_{i-1}$.

APPENDIX D: SEDOV SOLUTION

For the analytic solution to the Sedov problem, we rederived the solution given in Landau and Lifshitz's *Fluid Mechanics*, thereby finding the correction to the often remarked upon error (in an exponent) in that book's solution. The independent variables are t and r . In the similarity solution, lengths are measured with respect to the shock radius so that $r = R_s(t)$ corresponds to $\xi = 1$, where ξ is the similarity variable

$$\xi = r \left(\frac{\rho_o}{E_o t^2} \right)^{1/5}.$$

The preshock density is ρ_0 and the explosion energy is E_o . For the following equations, the fluid velocity (in the frame in which the centre of the remnant is at rest) is V and the local adiabatic speed of sound is c_s .

Define the dimensionless density, fluid velocity and sound speed squared

$$G(\xi) = \frac{\rho}{\rho_o}, \quad U(\xi) = \frac{5t}{2r} V, \quad Z(\xi) = \frac{25t^2}{4r^2} c_s^2.$$

Directly behind the shock,

$$G(1) = \frac{\gamma + 1}{\gamma - 1}, \quad U(1) = \frac{2}{\gamma + 1}, \quad Z(1) = \frac{2\gamma(\gamma - 1)}{(\gamma + 1)^2}.$$

A solution is

$$\begin{aligned} \xi^5 &= \left(\frac{\gamma + 1}{2} U \right)^{-2} \left(\frac{\gamma + 1}{7 - \gamma} [5 - (3\gamma - 1)U] \right)^{\nu_1} \times \\ &\quad \left(\frac{\gamma + 1}{\gamma - 1} (\gamma U - 1) \right)^{\nu_2} \\ G &= \frac{\gamma + 1}{\gamma - 1} \left(\frac{\gamma + 1}{\gamma - 1} (\gamma U - 1) \right)^{\nu_3} \times \\ &\quad \left(\frac{\gamma + 1}{7 - \gamma} [5 - (3\gamma - 1)U] \right)^{\nu_4} \left(\frac{\gamma + 1}{\gamma - 1} (1 - U) \right)^{\nu_5} \\ Z &= \frac{\gamma(\gamma - 1)}{2} \frac{U^2 (1 - U)}{\gamma U - 1} \end{aligned}$$

where

$$\nu_1 = -\frac{(13\gamma^2 - 7\gamma + 12)}{(2\gamma + 1)(3\gamma - 1)} \quad \nu_2 = \frac{5(\gamma - 1)}{2\gamma + 1}$$

$$\nu_3 = \frac{3}{2\gamma + 1} \quad \nu_4 = -\frac{\nu_1}{2 - \gamma} \quad \nu_5 = -\frac{2}{2 - \gamma}$$